CVC Tech.Rep. #089 August,2005

A Deterministic-Statistical Strategy for Adventitia Segmentation in IVUS images

Aura Hernàndez, Debora Gil, Petia Radeva

Dept. Ciències de la Computació UAB

Computer Vision Center, 2005

A Deterministic-Statistical Strategy for Adventitia Segmentation in IVUS images

by

Aura Hernàndez, Debora Gil, Petia Radeva

Abstract

A useful tool for some specific studies in cardiac disease diagnosis is vessel plaque assessment by analysis of IVUS sequences. Manual detection of luminal (inner) and media-adventitia (external) vessel borders is the main activity of physicians in the process of lumen narrowing (plaque) quantification. Difficult definition of vessel border descriptors, as well as, shades, artifacts and blurred signal response due to ultrasound physical properties troubles automated adventitia segmentation. In order to efficiently approach such a complex problem, we propose blending advanced anisotropic filtering operators and statistical classification techniques into a vessel border modelling strategy. Our systematic statistical analysis shows that the reported adventitia detection achieves an accuracy in the range of inter-observer variability regardless of plaque nature, vessel geometry and incomplete vessel borders.

1 Introduction

IVUS imaging is a unique imaging clinical tool [1] that provides cardiologists with a cross sectional inside view of the vessel (fig.1(a)) and, thus, allows a complete study of its morphology, such as arterial wall, lumen or plaque. The technique helps diagnosis and treatment of cardiac diseases, as far as a precise characterization and segmentation of arterial structures are available. A manual processing of images, apart from being a tedious time consuming task, might suffer from intra- and inter- observer variability. This fact motivates the development of image processing techniques addressing detection of arterial structures.

Since the early years, many algorithms for a reliable intima detection have been proposed ([2]-[7]). By its inherent difficulty (its distance from the ultrasound transducer reduces sharpness in the border visual appearance), adventitia modelling has been only approached in recent works ([8]-[17]). However, an accurate border detection requires either elaborated strategies in the case of contour based segmentations ([13]-[17]), or a previous plaque and tissue characterization in the case of classification strategies ([10], [11]). We argue that vessel borders detection should serve to characterize and quantify vessel plaque rather than following as a side result of a laborious plaque classification. In the present work, we describe an adventitia detection method based on a supervised learning of the boundary followed by a segmentation determined by its geometry.

Usual techniques addressing segmentation of vessel borders (intima and adventitia) rely on a single local image descriptor (usually edges) to guide a snake towards the target structures ([11],[14],[15],[17], or to minimize a cost function with dynamic programming ([3],[4],[13],[16]). Regardless of low quality in IVUS images, adventitia detection adds the difficulty of a large variety of descriptors, a weak visual appearance by a decrease in the ultrasonic pulse energy [19] and incomplete contours due to echo opaque plaques (e.g. calcium) shadowing. It follows that standard segmentation approaches do not suffice by their own and need ad-hoc strategies to yield proper results. Some authors [2]-[4], [16], [17] combine transversal and longitudinal contours to endow the model with spatial continuity along the sequence. In this case, the use of ECG-gated sequences [4], [10] significantly helps to achieve a reliable segmentation of longitudinal cuts. Other approaches ([5], [6], [10]) manually restrict a region of interest that serves to initialize a snake, although such initialization might need to be updated along the sequence.

A common inconvenience of segmentation based on contour detection is that it requires some kind of image filtering to avoid fake responses. The poor image quality as well as large variety of IVUS artifacts (calcium, shadows, catheter guide and blood back scatter) make standard anisotropic smoothing [30] fail to achieve optimal results. In order to overcome these drawbacks, several approaches have been proposed. The most simple strategy is to discard those images containing too much artifacts [13]. Although this is a practical way of filtering, it runs the risk of losing too much information for a reliable recovery of vessel borders. Others ([7],[18]), directly handle raw data (the ultrasound signal before being digitalized) and filter impulse responses of the transducer. Unfortunately, raw data acquisition needs a special device not always available in standard clinical equipments.

Recent approaches ([8]-[12], [20]) use classification strategies to better characterize coronary structures (plaque and vessel borders). Although results are robust to noise and artifacts, some of them ([8], [10], [20]) require a manual region of interest ([8], [10]) or an accurate segmentation of the first sequence frame for each different case ([20]).

Boundary detection in complex images should hinge on more than one image descriptor ([20], [34], [24]) and take into account level sets geometry ([27], [24]). The latest advances in the field ([20], [34], [24]) suggest the use of supervised classification techniques in order to learn the values that best characterize the boundary of interest. The deterministic-statistical strategy for adventitia detection we propose is a three-fold algorithm that combines supervised learning with geometric-based filtering and segmentation techniques. In a first preprocessing step, a restricted anisotropic diffusion [28] sharpens vessel borders appearance in the polar transform of each IVUS frame. In the second stage, supervised classification techniques serve to compute two binary maps: one for vessel borders and another one for calcium sectors. The latter in order to discard sectors of ambiguous information due to echo shadowing (calcium plaque in

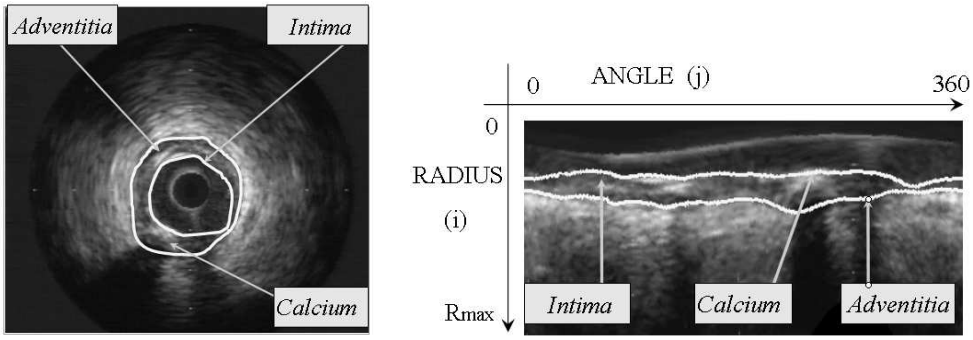

(a) (b)

Figure 1: IVUS images in cartesian (a) and polar (b) coordinates

fig.1(a)). In the last step, the fragmented vessel segments of the vessel mask are modelled by computing an implicit closed representation using an anisotropic contour closing [27] and, then, an explicit B-spline compact parameterization.

The topics are presented as follows. In Section 2 we outline the 3 main steps of the algorithm. Image preprocessing is detailed in Section 3, the selection stage is given in Section 4 and computation of a closed model in Section 5. Sections 6 and 7 are devoted to validation of the method (validation protocol and statistical results, respectively) and Section 9 to conclusions and further research.

2 General Strategy

The strategy for media-adventitia (simply adventitia from now on) segmentation we suggest summarizes in the following three main steps:

I. Image Preprocessing.

A. Polar Transformation of IVUS images — Advanced techniques for medical imaging segmentation [24] use *a priori* knowledge of the target structure shape. In the case of the adventitia border, its circular appearance can be imposed by simply transforming images to polar coordinates with the origin at the geometric center of the vessel border. In this coordinate system, the adventitia is nearly a horizontal curve, which significantly simplifies border feature extraction and parameterization.

B. Restricted Anisotropic Diffusion (RAD) — In order to enhance significant structures while removing noise and textured tissue, we use a Restricted Anisotropic Diffusion [28]. This filtering scheme modifies classic anisotropic diffusions [30] by suppressing any diffusion across image level curves. The associated image operator homogenizes image structures gray values according to their geometric continuity and, thus, results in a more uniform response to image local descriptors (edges, valleys, ridges).

II. Statistical Selection of Border Points.

The goal of the selection stage is to compute a mask of vessel borders segments and calcium sectors. Extracting vessel borders and calcium points requires defining the functions that best characterize each set, as well as, their most discriminating values. We learn, both, feature space and parametric threshold values by applying supervised classification techniques to a training set of manually segmented images.

A. Feature Space Design — Our feature space is designed to discriminate among the set adventitia/intima, calcium and fibrous tissue. Calcium discrimination is needed to discard angular sectors

of ambiguous information and fibrous tissue to avoid miss detections of vessel borders. By the polar coordinates chosen, horizontal edges are the main descriptors of the set adventitia/intima. Image simple statistics serve to formulate the functions characterizing calcium and fibrous plaque.

B. Extraction Parameters — In a segmentation procedure there are two kind of parameters, those that best discriminate among different structures in the feature space and those acting as a filter of fake responses. Discriminating parameters are thresholding values on the feature space, while length filtering removes spurious detections from the extracted segments. Both parameters are tuned to yield an optimal segmentation for a training set of manually traced borders.

III. Segmentation Stage.
The selection stage produces two binary images: adventitia/intima points and calcium sectors. Vessel border segments are modelled by computing an implicit closed representation and, then, an explicit snake representation using B-splines.

A. Implicit Anisotropic Contour Closing (ACC) — For the implicit closing we suggest using an Anisotropic Contour Closing [27] based on functional extension principles to complete curve segments in the image mask domain. The use of restricted diffusion operators enables to take into account image geometry, restore curved shapes and discard calcium and side branches sectors. We endow 3D continuity to such implicit reconstruction by simple morphological (reference) area considerations.

B. Explicit B-Snakes Representation — We define vessel contours at branching and calcified segments by approaching ACC with a B-spline snake. B-snakes yield a smooth representation encoded with N control points and conforming to the completion mechanisms of human vision [37].

3 Preprocessing

3.1 Polar Coordinates

In an IVUS plane, the adventitia border is an elliptic-like shape with a relatively small eccentricity (fig. 1(a)). By transforming images to polar coordinates (see fig. 1(b)), we have the following simplifications. Firstly, by its convexity, whatever the origin we take, the adventitia can be parameterized by the radius. This simplifies computation of the final snake model. Furthermore, if we take as origin its geometric center, the border transforms to nearly an horizontal line continuously varying along the sequence. The former simple shape allows the use of horizontally oriented image descriptors. Any deviation in the position of the geometric center introduces an undulation in the polar transform of the vessel structure (fig. 2(a)). Such eccentricity forces the use of a bank of filters and might trouble endowing 3D continuity to the final model in the case of a dynamic shape evolution along the sequence.

In non ECG-gated sequences there are two main sources of adventitia border eccentricity. A systematic spatial evolution (also observed in in-vitro pullbacks) of the lumen center induced by the vessel morpho-geometric characteristics. And a dynamical spatio-temporal vessel evolution caused by heart beating. Cardiac dynamics introduce four main artifacts: a longitudinal displacement of the catheter along the vessel (up to 2 mm), a dynamic tilting of the IVUS plane and a translation of the vessel followed by a rotation centered at the vessel center. By the smooth changes in vessel geometry and the low percentage of eccentricity introduced by catheter tilting, only the last two phenomena affect the proposed segmentation strategy. To be precise, in a polar domain with a fixed origin (e.g. the image center), any rigid transformation results in a dynamic radial wave (due to translation) followed by a horizontal (angular) translation. The first one is a main artifact and it is suppressed by processing the original image as follows.

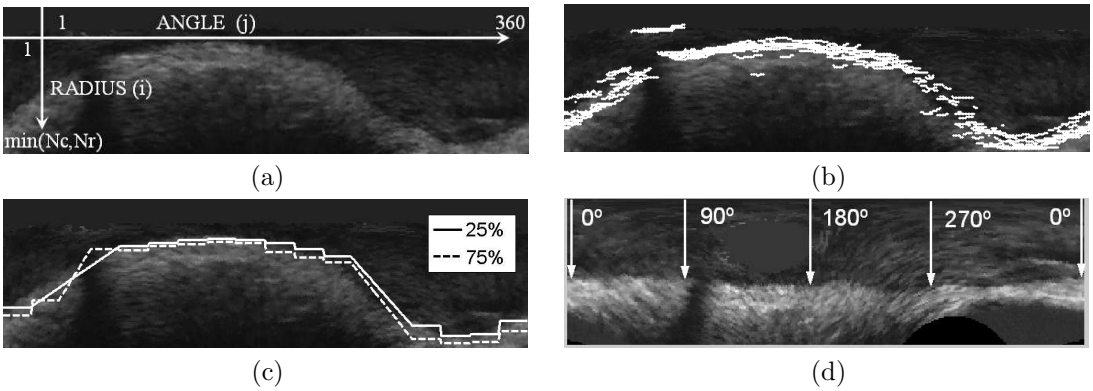

Figure 2: Adventitia Straighten Procedure: polar image with origin at the image mass center (a), edges in a sequence block (b), central percentile of edges positions (c) and final polar image (d).

Heart dynamics eccentricity is removed by taking as origin the image mass center. Since its coordinates are given by the weighted average of the image in cartesian coordinates,

$$\frac{1}{NcNr}(\sum_{i,j} iI(i,j), \sum_{i,j} jI(i,j))$$

it follows that its spatio-temporal evolution captures cardiac motion. Still, in such polar system (fig. 2(a)) the adventitia might present a static curved pattern if the iis not at the vessel center. This geometric eccentricity is reduced by computing the geometric mass center of a set of points roughly lying on the adventitia. Such points are extracted by means of negative horizontal edges (see Section 4 for the definition) of the polar image, namely e_y. The impact of noise and artifacts is minimized by splitting the sequence in blocks of N consecutive images and averaging e_y for each block. We note that because of heart motion we might not be averaging the same part of the tissue which produces a blurring of the energy average at curved angular sectors. The number of frames achieving the best compromise between small artifacts removing and tissue blurring is approximately a third of the heart cycle (10 frames in pull-backs at 30 frames per second). We select for each angle (column) those points with the former average below the 5% radial percentile (see Section 4.2 for details on its choice). Spurious edges due to noise and other sparse artifacts (such as blood scatter at branches) are removed by applying a morphological opening on the edge image that leaves only those connected components of a length above a given value. We adopt the same discriminant criterion as in Section 4.2 and, for each image, take the 3rd quartile of the statistical distribution of its edges length. In order to endow further continuity to the selected segments, we use the statistical distribution of their radial position along a block of images. Percentiles computed in the sequence blocks of 100 frames serve to discard outliers by only considering points within the central percentile range. In order to capture the adventitia curvature, percentiles are computed on angular sectors of 5 degrees (5 column wide). The final radial values serve to compute the new origin of our polar transform.

Figure 2 illustrates the main steps of the geometric eccentricity suppression. Fig.2(a) shows the polar transform with the origin at the image mass center with the usual undulation produced by an origin different from the vessel geometric center. Fig.2(b), the selected edges in a sequence block before percentile filtering and fig.2(c) shows the plot for their central percentile. The straightened adventitia image (fig.2(d)) has the catheter appearing at the center of the lumen in the second quartile of the image by its deviation from the vessel geometric center.

From now on, we will work with images in polar coordinates, namely $AdvPol(i,j)$. Rows, $i = 1,\ldots,\min(Nc,Nr)$ (for Nc, Nr the columns and rows of the IVUS image), represent the radius and columns, $j = 1,\ldots,360$, the angle.

3.2 Restricted Anisotropic Diffusion

Most filtering techniques based on image gray level modification [30] use the heat diffusion equation:

$$I_t(x,y,t) = \mathrm{div}(J\nabla I) \quad I(x,y,0) = I_0(x,y) \tag{1}$$

to de-noise an image $I_0(x,y)$. The time dependant function I is the family of smoothed images and J is a 2-dimensional metric (i.e. an ellipse) that locally describes the way gray levels re distribute. The diffusion tensor J is thoroughly described by means of its eigenvectors (ξ, $\eta = \xi^{\perp}$) and eigenvalues (λ_1, λ_2). If the latter are strictly positive, like in existing anisotropic filtering techniques ([29], [30]), gray values spread on the whole image plane and the family I converges to a constant image. But if we degenerate J and admit null eigenvalues ($\lambda_2 = 0$), then diffusion only takes place in the integral curves of the eigenvector (ξ) of positive eigenvalue [27]. Smoothing effects depend on the suitable choice of the eigenvector of positive eigenvalue. In the case that ξ is a smooth vector representing the tangent space to a closed model of the image level sets, then the final image is a collection of curves of uniform gray level [28].

The Structure Tensor [33] is a quick way of computing the guiding vector ξ that has already proven its efficiency [27]. The Structure Tensor, namely ST_ρ, is a gaussian mean of the projection matrices onto a regularized image gradient. That is, given a gaussian, G_ρ, of variance ρ and zero mean, the structure tensor is the following convolution:

$$ST_\rho = G_\rho * \left[\begin{pmatrix} I_x \\ I_y \end{pmatrix} (I_x, I_y) \right] = \begin{pmatrix} G_\rho * I_x^2 & G_\rho * I_x I_y \\ G_\rho * I_x I_y & G_\rho * I_y^2 \end{pmatrix}$$

for $(I_x, I_y) = G_\sigma * \nabla I$ the components of a regularized image gradient. The eigenvectors of the Structure Tensor represent a smooth extension of the image level sets tangent space ([27]). The scale σ controls the degree of gaussian image smoothing used to compute the initial tangent space and ρ the scope of the extension of such space. In order to preserve the detail in the continuous curves of the image, we recommend keeping σ as low as possible. As for the extension scale ρ, the range $\rho \in [1,2]$ achieves a good compromise between restoring closed models of continuous curves and keeping the random nature of texture and noise. The standard smoothing setting we recommend is $(\sigma, \rho) = (0.5, 2)$.

We use ST_ρ eigenvectors to design our diffusion tensor as follows. Let us consider a metric $\tilde{J}$ with eigenvalues $\lambda_1 = 1$ and $\lambda_2 = 0$, and ξ the eigenvector of minimum eigenvalue of ST_ρ. The Restricted Heat Diffusion we suggest is given by:

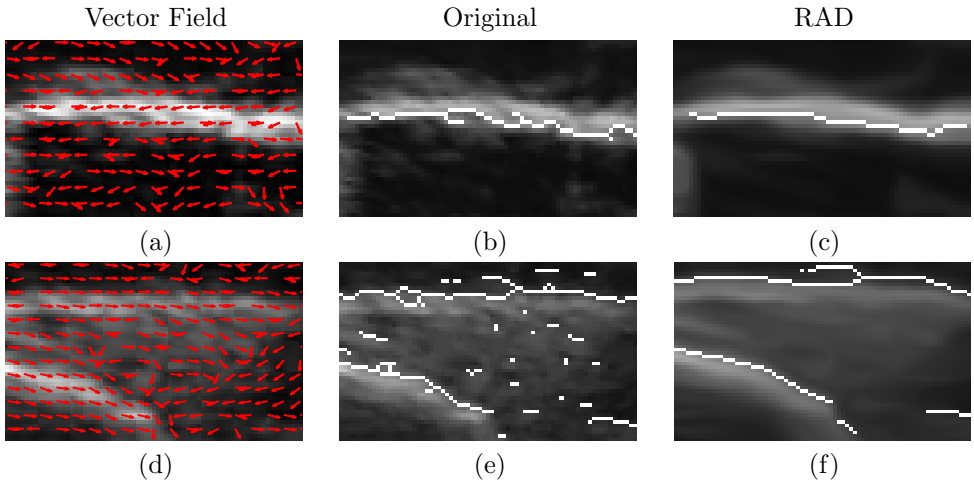

Figure 3: RAD smoothing for calcium (1st row) and adventitia (2nd row)

$$
\begin{aligned}
& I_t = \mathrm{div}(Q\tilde{\Lambda}Q^t\nabla I), \quad I(x,y,0) = I_0(x,y) \\
& \text{with } Q \text{ the eigenvectors of } ST_\rho = G_\rho * \left(\nabla I_\sigma \nabla I_\sigma^T\right), \\
& \tilde{\Lambda} = \begin{pmatrix} 1 & 0 \\ 0 & 0 \end{pmatrix} \quad \text{and} \quad \nabla I_\sigma = G_\sigma * \nabla I
\end{aligned}
\tag{2}
$$

Since the guiding vector, ξ, is oriented along image structures and randomly at textured and noisy areas, RAD smoothes image gray values along its regular structures and acts like a gaussian filter otherwise. The result is that solutions to (2) converge to a smooth image that has a uniform continuous response to standard detectors based on the image local descriptors. Figure 3 illustrates the mechanisms and effects of equation (2) in a calcified region (1st row) and near the intima and a fibrous tissue (2nd row). We applied a standard ridge detector to the calcium image and a horizontal edge operator to the intima/fibrous tissue one. The vector ξ depicted in fig.3(a) and (d) is well defined near the structures and randomly distributed in textured tissue (fig.3(d)) and the echo opaque shadow below calcium (fig.3(a)). The original response (fig.3(b), (e)) yields fragmented curves for the target structures and fake detections due to noise. In RAD images (fig.3(c),(f)), background spurious edges (fig.3(f)) have been removed, while the intima, the fibrous structure and calcium are regular closed curves.

4 Statistical Selection of Border Points

The inner and outer vessel borders appearance is so similar that they are assumed to constitute a single class in the training process. Their distinct radial position suffices to discriminate them [17] in the absence of echo opaque structures, such as calcium. In such cases, the adventitia does not appear and the detection is misled towards the intima. Hence the best solution is to discard echo opaque sectors, the training stage also addresses their characterization. We also include fibrous tissue discrimination because it is a main artifact confusing with the adventitia [17].

4.1 Feature Space Design

The feature space we propose is a three dimensional space tuned to describe the adventitia/intima set and echo opaque structures.

1. *Horizontal Edges*

   Since in the coordinate system chosen, the adventitia layer is a horizontal dark line, horizontal edges constitute our main descriptor. Edges are computed by convolving the image with the y-partial derivative of a 2 dimensional gaussian kernel of variance σ:

   $$
   \begin{aligned}
   & e_y(i,j) = g_y * AdvPol \\
   & \text{for } \; g_y(i,j) = -\tfrac{j}{2\pi\sigma^4} e^{-(i^2+j^2)/(2*\sigma^2)}
   \end{aligned}
   $$

   In order to keep the maximum accuracy in edges location, we set $\sigma = 0.5$.

   The only image structures yielding large values for e_y are intima, adventitia, calcium and fibrous tissue. Intima and adventitia correspond to negative values, while calcium and fibrous structures yield a negative and a positive response, one for each of their bordering sides.

   The descriptors we have chosen to detect echo opaque plaques and fibrous tissue are their outstanding brightness and, for calcium, the dark shadow underneath. We propose the following particular functions to quantify such features.

2. *Radial Standard Deviation*

   Striking brightness corresponds to an outlier of the pixel gray value in the radial distribution. We measure it by means of the difference between the pixel gray value and the radial mean. For each pixel (i, j), we define it as

   $$\sigma(i,j) = (AdvPol(i,j) - \mu(j))^2$$

   where $\mu(j))$ is the radial (i.e. column-wise) mean of the polar image:

   $$\mu(j) = \frac{1}{N_r} \sum_{i=1}^{i=N_r} AdvPol(i,j)$$

   The magnitude of σ is maximum at bright structures (calcium and fibrous plaque) and close to zero near the adventitia. In order to distinguish between calcium and fibrous plaque, we add the following shadows detector:

3. *Cumulative Radial Mean*

   For each column j consider the following cumulative mean:

   $$\tilde{\nu}_j(i) = \frac{\sum_{n=R_{max}}^{n=i} AdvPol(n,j)}{R_{max} - i}$$

   For angles with calcium, the function $\tilde{\nu}_j(i)$ presents a step-wise profile in contrast to a more uniform response in the presence of fibrous plaque. It follows that the total energy:

   $$\epsilon(j) = \sum_{i=1}^{i=R_{max}} \tilde{\nu}_j(i)$$

   achieves its minimum values only at sectors with calcium.

The feature space achieving a maximum separability for our training set is given by:

$$(X, Y, Z) = (e_y, sign(e_y)\sqrt{|e_y \sigma|}, \epsilon)$$

4.2 Statistical Parameter Setting

For the computation of the vessel borders and calcium binary images, the classification problem we must face is discriminating among 4 different sets: adventitia/intima (Adv), calcium (Cal), fibrous structures (Fbr) and the rest of pixels (RP). Instead of addressing the 4-class problem as a whole, we will solve several 2-class problems in 2 dimensions.

For its simplicity and proven efficient performance, our main classifying tool will be Fisher linear discriminant analysis [31]. Linear Discriminant Analysis searches for the linear subspace, W, that achieves a maximum separability among the projected classes. In the case of Fisher, separability is measured in terms of maximum separation between class means and minimum within-class scatter. Mathematically, this criterion is formulated in terms of the ratio between the between-class, S_B, and the within-class, S_W, scatter matrices:

$$\mathbf{S_B} = \sum_{\mathbf{i=1}}^{\mathbf{c}} (\mu_\mathbf{i} - \mu)(\mu_\mathbf{i} - \mu)^\mathbf{t}$$
$$\mathbf{S}_W = \sum_{\mathbf{i=1}}^{\mathbf{c}} \sum_{\mathbf{j=1}}^{\mathbf{N_i}} (\mathbf{Y_j} - \mu_\mathbf{i})(\mathbf{Y_j} - \mu_\mathbf{i})^\mathbf{t}$$

for c the number of classes, N_i the samples per class, μ_i the mean vector of each of them and μ the mean of all samples (Y_j). Fisher discriminant criterion reduces to finding the subspace, W, maximizing:

$$J(\mathbf{W}) = \frac{|\mathbf{W}^t \mathbf{S}_B \mathbf{W}|}{|\mathbf{W}^t \mathbf{S}_W \mathbf{W}|}$$

Because S_B encodes the projection onto the linear subspace given by $\mu_1, \ldots, \mu_c$, it has, at most, rank $c-1$, which bounds W dimension by $\dim W \leq c-1$. In the particular case of a 2-class problem in 2 dimensions, Fisher space is a straight line (solid line in fig.4) and discrimination between the two classes is achieved by a threshold on the projection space.

We will use a Bayesian approach [31] to select thresholding values in terms of miss classification errors. In the two class problem, the classic Bayesian strategy searches for the value that achieves a suitable compromise between the percentage of false positives and false negatives. The approach selects a threshold in terms of how many true positives are detected without considering the amount of noise introduced in the positive detections. Although the criterion is widely used in classification problems, in the case of severe unbalanced classes or object segmentation [34] it is more efficient to select thresholds in terms of the trade-off between precision and recall.

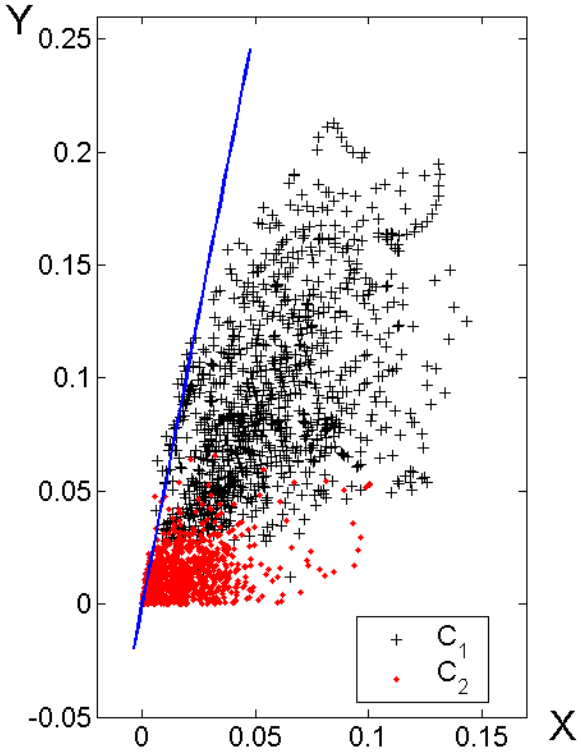

Figure 4: Feature Space for Adventitia (C_2) vs Brilliant Structures (C_1) Discrimination

This is the strategy we propose for the computation of the Adv and Cal mask images.

A. **Vessel Borders Mask.**

Borders extraction is achieved by addressing 2 classification issues: discriminate C_1=(Adv,RP) and C_2=(Cal, Fbr) in the (X, Y) plane and, then, separate Adv from RP using X values.

We discriminate C_1 (positives) and C_2 (negatives) by projecting onto the Fisher space, $PF1$, (see fig.4) and tuning the standard Bayesian threshold. Since our discriminating problem is detecting as much adventitia points as possible, we select the value, τ_{PF1}, that, among all thresholds ensuring at least 90% of C_1 detections yields optimal segmentation results. Discrimination between Adv and RP is achieved in the X coordinate domain, as Adv corresponds to large negative values. Large range of Adv values among different patients, suggests the use of an image sensitive threshold rather than a common value for all cases. We adopt a strategy in the fashion of discriminant snakes [20], [22] and select a different value for each column. Radial (column-wise) percentiles (ρ_X) are used to compute such threshold. Finally, small

structures in the vessel borders image are removed by applying a length filtering, so that only segments of length above a given percentile (ρ_L) are kept (see subsection 7.1 for a detailed explanation).

If we note by $PF1$ the projection of the (X, Y) space onto the Fisher line, then, for every frame, points are labelled as Adv if they fulfill:

$$PF1 < \tau_{PF1}, \quad X < \rho_X$$

and their segment length is above ρ_L. Figure 5 (b), (c) illustrates the extraction of adventitia/intima points. In fig.5(b) we have the output of the discrimination step and in fig.5(c) the result after applying a length filtering.

B. **Calcium Mask.**

The feature space chosen to discriminate calcium from fibrous tissue is given by the projection $PF1$ and the Z coordinate. A threshold on the Fisher space, $PF2$, for the 2D space $(PF1, Z)$ separates Cal and Fbr. Instead of following a Bayesian approach we will follow a precision-recall criterion and among all thresholds admitting, at most, a 10% of noise select the value, τ_{PF2}, that ensures a better segmentation of our training set.

It follows that, calcium points are those pixels that satisfy:

$$PF1 \geq \tau_{PF1} \quad \text{and} \quad PF2 > \tau_{PF2}$$

The thresholding parameters (τ_{PF1}, ρ_X, ρ_L and τ_{PF2}) hinge on the ultrasonic acquisition device characteristics. The specific values for the device used in our experiments are given in the experimental Section 7.

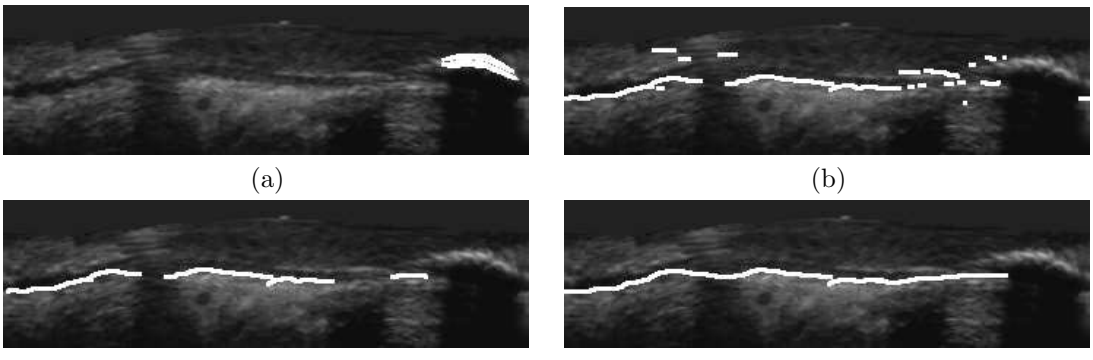

(a) (b) (c) (d)

Figure 5: Vessel Borders Point Extraction: calcium mask (a), adventitia mask resulting from the classification (b), adventitia mask after length filtering (c) and ACC closing (d)

5 Closing Stage

The selection stage produces two mask (binary) images: one for calcium (fig.5(a)) and another one for vessel borders (fig.5(c)). In the case of non circular patterns (caused by either catheter tilting or vascular modelling in eccentric plaques), the adventitia mask might result in a sparse collection of fragmented curve segments which omits the most curved sectors of the border. In order to correctly restore the vessel geometry, while recovering a smooth representation, we close the adventitia layer in two steps.

5.1 Implicit Anisotropic Contour Closing

Heat diffusion has the property of smoothly extending a function defined on a curve in the plane, provided that boundary conditions are changed to Dirichlet [32]. By using restricted heat operators this property

can be used to complete unconnected contours [27] as follows. Let γ be the set of points to connect, χ_γ its characteristic function (a mask) and define $\tilde{J}$ as in RAD (2), then the extension process:

$$u_t = \text{div}(\tilde{J}\nabla u) \quad \text{with} \quad u_{|\gamma} = u_0 \tag{3}$$

converges to a close model of γ. Intuitively, we are integrating the vector field ξ, that is, we are interpolating the unconnected curve segments along it. This fact not only ensures convergence to a closed model, but also yields closures more accurate than other interpolating techniques (such as geodesic snakes) which, at most, yield piece-wise linear models.

For adventitia completion the vector ξ is the eigenvector of minimum eigenvalue of the Structure Tensor computed over the edge map e_y. In order to avoid wrong continuations at side branches, sensor shadows and calcium sectors, the vector ξ is weighted by a function w_ξ:

$$w_\xi(i,j) = \begin{cases} 0, & \text{if } (i,j) \in \text{Calcium} \\ coh = \frac{(\lambda_1-\lambda_2)^2}{(\lambda_1+\lambda_2)^2}, & \text{otherwise} \end{cases}$$

for λ_1, λ_2, ST_ρ eigenvalues with $\lambda_1 \geq \lambda_2$. At regions where ξ is a continuous vector, λ_2 is close to zero, so *coh* is maximum. Meanwhile, at noisy areas, since ξ is randomly oriented, λ_1 compares to λ_2 and $coh \sim 0$. This avoids miss interpolations at side branches and underneath the guide wire, provided we use the fast algorithm sketched in [17].

In order to endow 3D continuity to the final model, we apply a morphological opening (area filtering) of the surface given by blocks of N consecutive ACC closings.

5.2 B-snake Representation

Although ACC closure already contains all available information, by the discrete implementation used, the implicit model is an irregular step-wise model that still presents gaps at side branches and calcium sectors. Besides, the amount of images involved in the sequence suggests searching for a contour representation as compact as possible. This motivates guiding a parametric B-snake towards ACC closure to obtain a compact smooth explicit representation. A parametric snake is a curve $\gamma(u) = (x(u), y(u))$ which, under the influence of an external force, E_{ext}, and internal constraints, E_{int}, minimizes the energy functional:

$$E(\gamma) = \int_\gamma (E_{int}(\gamma) + E_{ext}(\gamma, \gamma_\tau))du = \int_\gamma (\alpha\|\dot{\gamma}\|^2 + \beta\|\ddot{\gamma}\|^2 + E_{ext}(\gamma, \gamma_\tau))du \tag{4}$$

where γ_τ is the curve to model and $\alpha, \beta \in [0,1]$ weight the trade off between the elasticity and stiffness of the snake. The external energy is a functional achieving a minimum on γ_τ.

In polar coordinates, as the adventitia is convex, we have that $\gamma = (\theta(u), R(u))$ can be represented as a function of the angle, $R = R(\theta)$, so that the functional simplifies to:

$$E(R(\theta)) \quad = \quad \int_1^{360} (\alpha\|R_\theta\|^2 + \beta\|R_{\theta\theta}\|^2 + (R - R_\tau)^2)d\theta$$

for R_τ the radius of the target curve and R_θ, $R_{\theta\theta}$ the first and second derivatives of the radius. If we parameterize with a B-Spline given by N control points:

$$R(\theta(s)) = R(s) = \sum_i c_i(s)R_i, \ \text{ for } s \in [0, N-1] \tag{5}$$

the functional (5) converts to a function of the N control points, with the minimum defined by:

$$\frac{\partial E}{\partial R_j} = 0, \forall j \in \{1, \ldots, N\} \tag{6}$$

Since the jth equation is:

$$\left(\frac{2\alpha}{\lambda^2}\right)\sum_i\left(\int \dot{c}_j\dot{c}_i\right)R_i+\left(\frac{2\beta}{\lambda^4}\right)\sum_i\left(\int \ddot{c}_j\ddot{c}_i\right)R_i+\sum_i\left(\int c_jc_i\right)R_i=\int c_jR_\tau \tag{7}$$

the system (5) admits a matrix formulation given by:

$$(B_1+B_2+B_0)R=BR=F_\tau \tag{8}$$

The entries of B_j are sums of the jth derivatives of the spline coefficients c_i. The term (B_1+B_2) corresponds to the stiffness matrix for B-splines snakes and B_0 is the extra term coming from our particular external energy. The forces F_τ induced by the target curve are computed via the parameter change $R_\tau(\theta(s))$, for $\theta(s)=\sum_i c_i(s)\theta_i$.

Equation (8) can be either solved iteratively (gradient descent of the energy (5)) or, since F_τ does not depend on R, given by the matrix inversion, $R=B^{-1}F_\tau$. In the first case, the initial snake should be the maximum radius of all points of the ACC mask. In case of using the explicit solution, the target radius is defined, for each angle, as the maximum radius along the i-essim column corresponding to such angle. The cartesian transform of the polar spline given by the above radial control points is our final adventitia model.

6 Validation Protocol

6.1 Study Group

We have validated our strategy in sequences captured with a Boston Scientific Clear View Ultra scanner at 40 MHz with constant pull-back at 0.5 mm/sec and acquisition rate of 25 frames/sec. The digitalized sequences are 384×288 images with a spatial resolution of 0.0435 mm per pixel. The study group has been designed to assess the ability of the reported algorithm to detect the adventitia border in the presence of different plaques, artifacts and vessel geometries. A total number of 5400 images extracted from 11 different cases have been tested. The sequences analyzed are clinical cases of the Hospital Universitari Germans Trias i Pujol in Badalona (Spain). We have segmented 22 vessel segments of a length ranging from 4 to 6 mm (200-300 frames) and including:

- segments with uncomplete vessel borders due to side-branches and sensor guide shadows,
- calcified segments,
- segments with non calcified plaque,
- normal segments.

All segments analyzed were catheterized before any interventional procedure which excludes stented segments. The method proposed was designed to fit the needs of the clinical team we work with, which major concern is to use the adventitia border to assess the vessel diameter and decide the viability and adequacy of an angioplasty. In addition, some stent designs may obscure the EEM border and render measurements unreliable [36].

For each segment, the adventitia has been manually traced every 10 frames by 4 experts in IVUS image interpretation, which yields a total number of 540 validated frames with 4 different manual models each. Our database for adventitia modelling validation might be obtained contacting aura@cvc.uab.es.

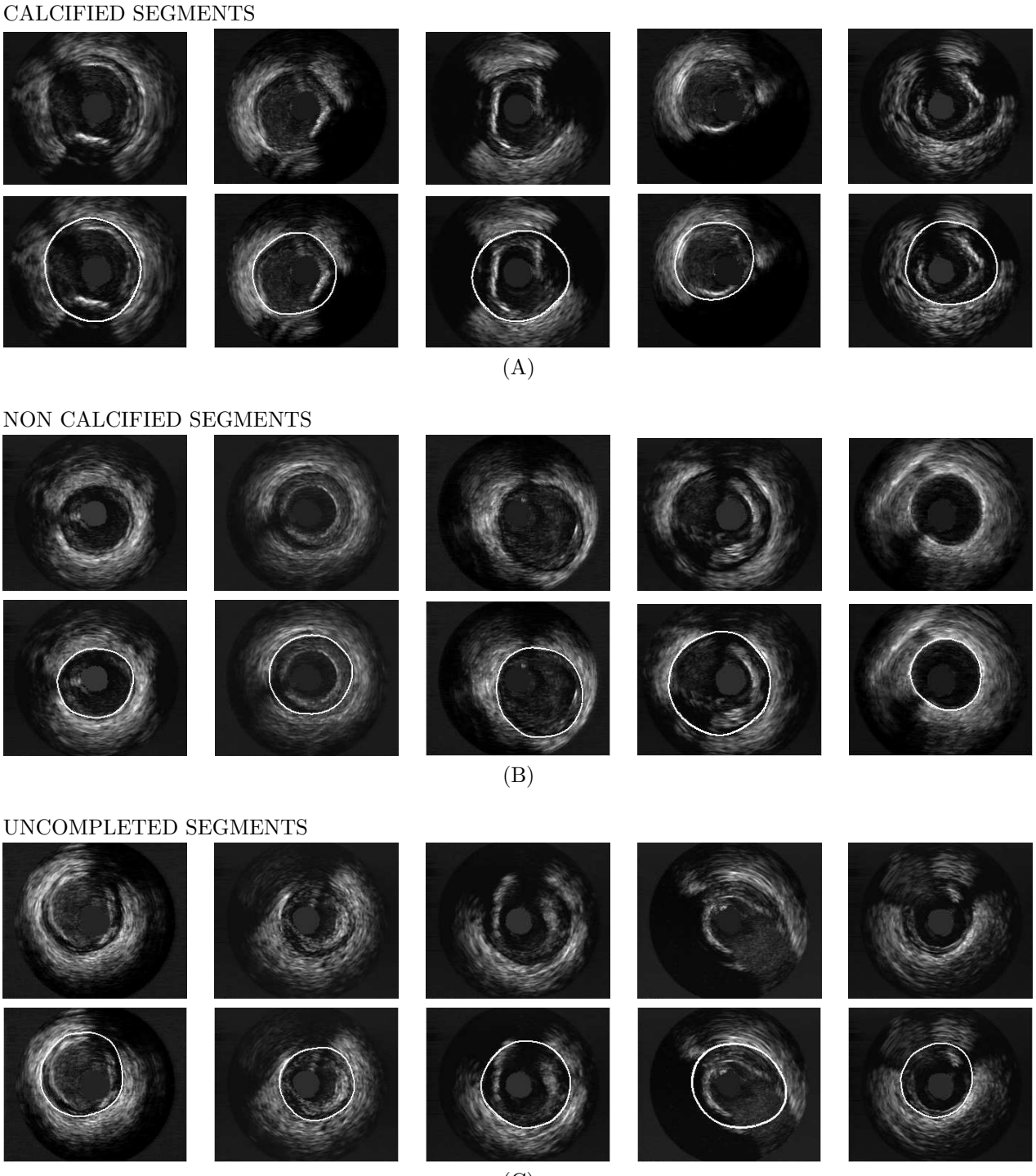

Figure 6: Automated Adventitia Detections: Calcified segments (A), non-calcified plaques (B) and uncompleted vessels (C)

6.2 Accuracy Measures

To assess the segmentation accuracy, the automatically detected borders have been compared to the manual models. Accuracy is quantified with the following standard measures:

1. *Absolute and Signed Distances.*

   Distance maps to manual contours serve to compute the difference in position between automatic and manually traced curves. Such maps encode for each pixel, $p = (x_p, y_p)$, its distance to the closest point on the manual contour:

   $$D(p) = \min_{q\in\gamma}(d(p,q)) = \min_{q\in\gamma}\left(\sqrt{(x_p - x_q)^2 + (y_p - y_q)^2}\right) \tag{9}$$

   where q are points on the manually identified contour. Signed distances ($SgnD$) [26] weight the value $D(p)$ depending on wether the pixel p lyes inside or outside the target curve γ. Its mean value detects any bias in curve position, that is, wether detections are systematically bigger or smaller than manual segmentations.

   We will consider absolute (in mm) and relative (in %) distance errors. Absolute errors are given by formula (9), while relative ones are the ratio:

   $$RelD(p) = 100 \cdot \frac{D(p)}{d(q,O)}$$

   where the origin, O, is the mass center of the manual contour and q is the point achieving the minimum in (9). Since relative errors take into account the true dimensions of the vessel, they reflect positioning errors better.

   For each distance error, its maximum and mean values on the automated contour are the error measures used to asses position accuracy. If PixSze denotes the image spatial resolution and p is any point on the automatically traced adventitia, then the set of functions measuring accuracy in positions are:

   - **Maximum distance errors** (in mm and %):

     $$MaxD = \max_p (D(p) \cdot PixSze)$$
     $$RMaxD = \max_p (RelD(p))$$

   - **Mean distance errors** (in mm and %):

     $$MD = \text{mean}_p (D(p) \cdot PixSze)$$
     $$RMD = \text{mean}_p (RelD(p))$$

   - **Mean signed distance error** (in mm):

     $$MSD = \text{mean}_p (SgnD(p) \cdot PixSze)$$

2. *Area Differences.*

   Binary images of manual, $I_M(i,j)$, and automatic, $I_A(i,j)$, borders serve to compute the following measure for area accuracy:

   - **Percentage of Area Differences**

     $$AD = 100 \cdot \frac{\sum_{i,j} |I_M(i,j) - I_A(i,j)|}{\sum_{i,j} I_M(i,j)}$$

Table 1: Comparison of Segmenting Parameters

	$TH1: 0.0578$ $TH2:$ -0.1295	$TH1: 0.0619$ $TH2:$ -0.1295	$TH1: 0.0567$ $TH2:$ -0.1241	$TH1: 0.0567$ $TH2:$ -0.01468	$TH1: 0.0567$ $TH2:$ -0.1295
Area 100	0.201 ± 0.046	0.201 ± 0.045	0.234 ± 0.093	0.234 ± 0.088	0.231 ± 0.089
Area 150	0.200 ± 0.045	0.200 ± 0.045	0.227 ± 0.082	0.230 ± 0.082	0.227 ± 0.081
Area 200	0.203 ± 0.045	0.220 ± 0.056	0.219 ± 0.069	0.230 ± 0.083	0.219 ± 0.069
Length 80 (%)	0.227 ± 0.060	**0.199 ± 0.041**	0.203 ± 0.043	0.204 ± 0.048	0.203 ± 0.043
Length 85 (%)	0.240 ± 0.070	0.237 ± 0.064	0.202 ± 0.044	0.203 ± 0.044	0.206 ± 0.048

The interval given by the mean ± standard deviation computed over the 4 experts contours indicate the statistical range of values for each of the automated errors (MaxD, RMaxD, MD, RMD and AD). However, accuracy in models strongly depends on the pixel resolution as well as on the (manual) visual identification of the adventitia layer. These dependencies have two main consequences. The first one hinders any comparison to other segmentation algorithms as the minimum error (in mm) depends on pixel precision. The second one, implies that an analysis of automated errors might not reflect, by its own, the true accuracy of segmentations, since a large variation range might be caused by a significant difference among experts models. A standard way [35] of overcoming the above phenomena is by comparing automated errors to the variability among different manual segmentations (inter-observer variability). Student T-tests are used to determine if there is any statistical significant difference between inter-observer and automated distance errors.

7 Results

Experiments also focus on determining the best set of discriminant and filtering parameters in a training stage and assessment of the whole strategy on a test set.

7.1 Parameters Study

Filtering parameters remove spurious fake detections from the discrimination stage. There are two main candidates to act as filtering parameters of the vessel borders masks, length filtering and area filtering. An exhaustive study determine which is the best set of parameters achieving an optimal segmentation of manually segmentation traced borders. Parameter learning is performed by analyzing mean and maximum absolute segmentation errors for a training set of 13 vessel segments which are representative of all kinds of plaques and vessel morphologies. The parameters to contrast are, on one hand, filtering parameters and, on the other hand, discriminating parameters. Table 1 summarizes the statistics for the best mixtures of thresholds ($TH1$, $TH2$). It follows that the set of optimal parameters for a Boston Clear View is given by the projections:

$$PF1 = 0.1906X + 0.9817Y \quad \text{and} \quad PF2 = -0.1498PF1 + 0.9887Z$$

with the thresholds for computation of vessel borders and calcium masks set to:

$$\textit{Vessel borders:} \quad TH1 = 0.0619;\ PRCT_X = 6\%;\ PRCT_L = 80\%$$

$$\textit{Calcium:} \quad TH2 = -0.1295$$

The adventitia detection parameters ensure a 99.95% of true C_1 detections. We note that, by the feature space definition, we only have a 15% of false positives, which just represent 6% of the total

number of points classified in C_1. This fact favors the use of an area filtering on adventitia detections as fake response remover. In the case of calcium extraction, the threshold achieves less than a 1% of noise and ensures 99.9678% of calcium detections. For the computation of the final B-snake model we have used 30 control points uniformly placed every 12 angles.

Table 2: Performance Evaluation of the Adventitia Segmentation Strategy. Automatic Errors versus Inter-Observer Variability for non-calcified and calcified segments

	NON-CALCIFIED		CALCIFIED	
	INT-OBS	AUT	INT-OBS	AUT
MaxD (mm)	0.4208 ± 0.1794	0.4238 ± 0.1026	0.6627 ± 0.3610	0.7161 ± 0.2532
RelMaxD (%)	0.3963 ± 0.1788	0.3868 ± 0.1075	0.5469 ± 0.3171	0.6116 ± 0.2665
MeanD (mm)	0.1783 ± 0.0698	0.1864 ± 0.0364	0.2650 ± 0.1306	0.2885 ± 0.0947
RelMeanD (%)	0.1647 ± 0.0668	0.1684 ± 0.0387	0.2142 ± 0.1113	0.2388 ± 0.0931
Area Dif. (%)	6.6799 ± 3.1579	7.2571 ± 1.9842	9.3511 ± 5.7529	10.0428 ± 4.0390
SgnMeanD (mm)	0.0004 ± 0.0769	0.0283 ± 0.0540	0.0163 ± 0.1213	-0.0381 ± 0.0912

Table 3: Performance Evaluation of the Adventitia Segmentation Strategy. Automatic Errors versus Inter-Observer Variability for all segments

	TOTAL	
	INT-OBS	AUT
MaxD (mm)	0.5386 ± 0.3075	0.5715 ± 0.2296
RelMaxD (%)	0.4697 ± 0.2664	0.5122 ± 0.2344
MeanD (mm)	**0.2206 ± 0.1126**	**0.2265 ± 0.0688**
RelMeanD (%)	0.1888 ± 0.0945	0.1972 ± 0.0662
Area Dif. (%)	**7.9813 ± 4.7962**	**8.6032 ± 3.3436**
SgnMeanD (mm)	0.0081 ± 0.1013	**0.0041 ± 0.0801**

Some of the adventitia segmentations achieved with the presented strategy are shown in figure 6. The first row (fig.6(A)) corresponds to images with calcified plaque. Images in the second row (fig.6(B)) have been extracted from non-calcified vessel segments, non-fibrous plaques in the first four images and a normal segment in the last one. Finally, images with missing information are shown in the third row, sensor guide shadows in the first three and side branches in the last two. We note that since B-snakes yield a curve that smoothly interpolates (up to the second derivative) vessel contours at the branch, in some cases the model resembles a circular-elliptical shape. This is the case (such as in fig.6 (C), #4-5) if the extreme points at the branch gap have equal radius and horizontal tangent vector in the polar domain.

7.2 Statistics

Figure 7 shows whisker boxes for mean distance absolute errors (fig.7(a)) and mean inter-observer variations (fig.7(b)) for a representative sample of soft plaque and calcium segments. Each box contains the

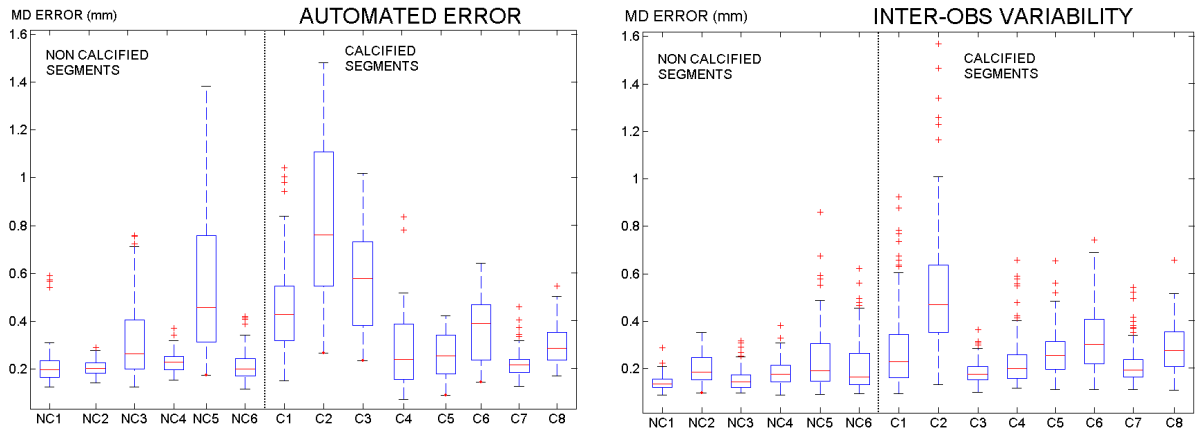

Figure 7: Whisker Boxes for Automated Error,(a), and Inter-Observer Variability, (b).

mean distance errors obtained from the 4 experts segmentations (80 to 120 samples per box) for a single vessel segment. Boxes labelled with **NC** correspond to non-calcified segments and those labelled with **C** to calcified ones. An analysis of the whisker boxes reflects robustness of segmentations: the smaller the boxes are, the more reliable the method is. Whisker boxes serve to visually detect any anomaly in the models. In general terms, the means of automated errors are slightly higher than inter-observer variability means. However, since automatic segmentations present a significantly smaller variation range than inter-observer variability, our segmentations are within the experts discrepancy rate (see T-tests comparing means summarized in table 4). Lack of reliable information at large angular sectors, significantly increases errors variability in calcified segments,both for manual segmentations and automatic detections. The large range of the whisker box of the case C2 detects it as a vessel segment of difficult manual identification that should be excluded from any statistical analysis. Larger boxes for automated detections (fig.7(a)) in cases NC5 and C3 comparing to their counterparts in fig.7(b) indicate that there are specially difficult cases for our segmenting strategy. We devote the next section to a detailed analysis of such miss detections.

Statistical ranges (mean $\pm$ standard deviation, computed for the 4 experts contours) for automatic errors (AUT) and inter-observer variability (INT-OBS) are summarized in tables 2 and 3. Patients presenting an unusual large inter-observer variability have been excluded, since we consider they are anomalous cases with difficult and non robust manual identification. We present statistics for non-calcified segments in the first column and calcified ones in the second column of table 2. A total population of 20 vessel segments is presented in table 3. A summary of the results of the T-tests comparing the inter-observer variability and automatic errors averages is given in table 4. We report the p-value and the confidence interval for the difference in means. Statistics exclude outliers (15% of the images, approximately) and T-tests are computed over the total errors in table 3.

According to a two tailed T-test, there is no significant difference between inter-observer and automated mean absolute distance errors and difference in areas. For mean distance errors the p-value equals $p = 0.177721$ and the confidence interval for the true difference in means at a significance level of 95% is $CI = (-0.002684, 0.014491)$. In the case of percentage in area difference, $p = 0.153404$ and the interval (also at a significance level of 95%) is $CI = (-0.017985, 0.114350)$. Maximum errors for automated detections are slightly above the range of maximum inter-observer variability. In order to robustly determine the fraction of increase, we use a single tailed T-test to check if the null hypothesis statement "the mean of automated maximum errors is above λ times the mean of maximum inter-observer variabilities" is true. The true proportion between maximum automated error and inter-observer variability

Table 4: Statistics Summary on T-tests comparing the means of Inter-Observer Variability and Automatic Errors.

	Confidence Interval (CI)	p-value
MeanD	(-0.002684,0.014491)	0.177721
Area Dif.	(-0.017985,0.114350)	0.153404
SgnMeanD	(-0.002401,0.010787)	0.212219

is between the minimum λ rejecting the null hypothesis and the maximum accepting it. For $\lambda = 1.102$, the null hypothesis was accepted with a p-value, $p = 0.053901$ and for $\lambda = 1.103$, it was rejected with $p = 0.049846$. We conclude that the increase in maximum automated errors is under a 10.3%. Finally a T-test on the mean of the automated signed distance error shows that in average it is zero as the p-value equals $p = 0.212219$ and the confidence interval for the true mean is a tiny interval containing the zero value $CI = (-0.002401, 0.010787)$.

8 Discussion

The combination of a priori knowledge (classification techniques) with filtering techniques based on continuity of image geometry is the key point for a robust characterization of vessel (the adventitia layer, in our case) borders. By designing an accurate point selection strategy, we avoid human interaction and the use of longitudinal cuts and ECG-gated acquisitions. The reliability of the proposed strategy is reflected in the global statistics extracted from in vivo sequences segmentation. The fact that, both, mean distances and vessel areas compare to inter-observer variation validates our method for extraction of clinical measurements. Since there is no bias in automated segmentations (the mean signed distance is statistically zero) we can ensure that our method achieves an optimal compromise among experts criteria as automatically traced curves lie between the curves traced by different observers. The number of outlier bad segmentations requiring manual correction represent less than a 15% of the studied valid cases.

Still, the striking increase in the error range for the anomalous cases NC5 and C3 needs to be analyzed. Such miss detections correspond to vessel segments that either the adventitia is hardly identified or there is severe lack of valid information.

Weak visual appearance of the adventitia border is a technical limitation of the UltraSound acquisition technique and it is cause of disagreement among experts (case C2 in fig.7(b)) in 9% of the cases. Our strategy suffers this kind of error in 18% of the segments under study (boxes C5, NC2 and NC3 in fig.7(a)). We argue that the only way to minimize the impact of border blurring is taking into account tissue motion periodicity along the sequence. Even for physicians it is difficult to identify vessel borders by an analysis of still images. Often, they use cardiac periodicity in the movement of vessel structures to distinguish between tissue and other structures. We are currently assessing if adding Fourier analysis of image grey level statistics to the set of adventitia descriptors reduces the number of this type of wrong detections.

Lack of information at calcium and side branches sectors, distorts measurements [36] and is a main source of error in automated models if the sparse valid information is not uniformly distributed. Images in fig.8 are representative of such source of variability in manual models and show the error introduced in automated segmentations. In the first column, we show the IVUS plane (fig.8(a), (f)), in the second one, the manual borders traced by two different experts (fig.8(b), (g)), in the third one, ACC closure (fig.8(c), (h)) and, in the last two, the B-snake model (fig.8(d), (i)) and its comparison to manual borders fig.8(e), (j)). The manual models significantly differ at those sectors were either echo shadowing

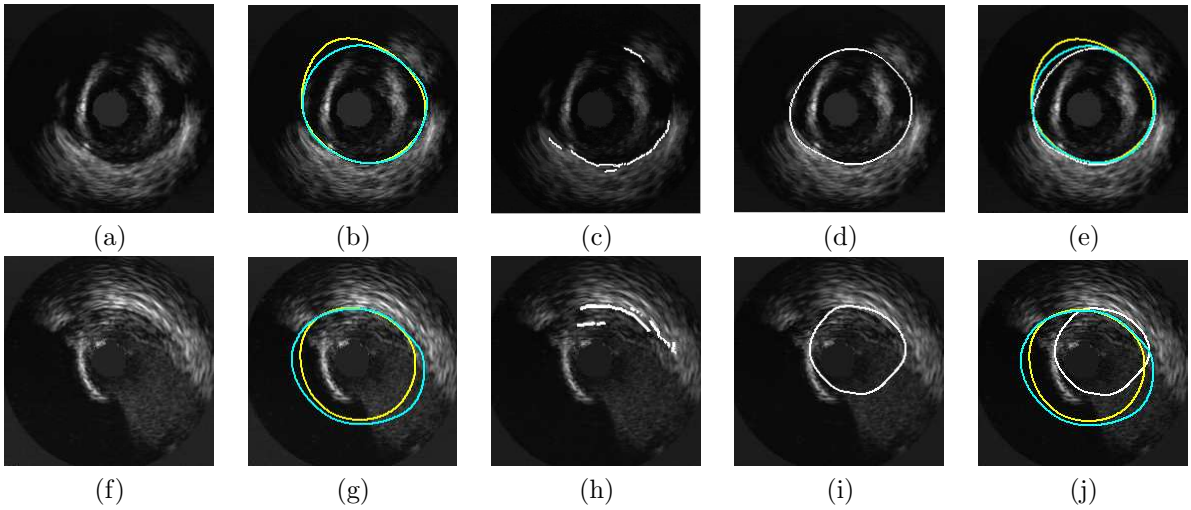

Figure 8: Adventitia models in images with sparse information. IVUS images (a), (f), manual models (b), (g), ACC (c), (h), final snake (d), (i) and comparison to manual models (e), (j).

(2nd and 3rd quartiles in fig.8(b) and (g), respectively) or blood (4th quartile in fig.8(g)) hide the adventitia border, which invalidates them for any reliable measurements. In the case of automated detections, models extracted from frames with uniformly distributed information (fig.8(d)) adjust to reference contours (fig.8(e)) although their error is prone to increase due to the higher disagreement among experts. Meanwhile, in the case of having all available information gathered in one of the image quadrants, the automated model (fig.8(j)) accuracy drastically drops (fig.8(j)).

We note that it is reported in the literature [36] that measurements should not be reported if lack of information is more extensive than 90 of arc. Still our error analysis prompts that lack of strong 3D continuity in the B-snake closing of candidate points on the vessel borders is the main source of the above error. The use of 2D NURBS (spline surfaces) instead of 1D splines could reduce the impact of missing information. However, in our case, they might not succeed in correcting this kind of miss interpolations. On one hand, NURBS can only take into account local deformations and continuity of the surface. On the other hand, the previously described pathology is prone to happen at large vessel segments. It follows that NURBS interpolation might imply handling the segmentation of the whole image sequence block (over 1200 frames), which is computationally unfeasible. One possible way of overcoming lack of information for large vessel segments would be mimicking the experts strategy used for manually tracing the adventitia borders. Our application [21] to manually segment vessel borders shows the previous border on the current image to be segmented and allows the physician to modify it. An informal survey on the key points and frames used by the expert for border tracing at images with severe lack of information prompts that they usually keep the model traced on the last valid frame. This suggests using the information available at the last frame with adventitia points detected in more than 70% of the vessel angular sectors to complete vessel borders at images with sparse detections.

9 Conclusions

Vessel border detection is of especial interest for plaque assessment and quantification of lumen narrowing in IVUS sequences. By its weak appearance, there are few algorithms addressing segmentation of the external adventitial border. In this paper we propose a general strategy for vessel border detection in IVUS images with an explicit application to the segmentation of the medial-adventitial border.

The reported methodology combines classification techniques with advance smoothing operators based on image level sets continuity. The strategy for media-adventitia detection is a three-step algorithm. We show that using geometric knowledge of image structures suffices to detect the adventitia without precise and exhaustive classification of vessel tissue. Besides our segmenting strategy is robust against a large variety of vessel cases, such as presence of different plaques, side-branches, IVUS artifacts (echo shadowing, sensor guide) and lost of information.

The strategy has been tested on 5400 images including calcified and non calcified vessel segments, side-branches and the most representative shadowing artifacts of intravascular ultrasound sequences. The comparison to borders manually traced by 4 experts shows that in 84% of the cases we are within the range of inter-observer variability, which demonstrates the optimality of the automated model. An exhaustive analysis of those cases increasing the error rate determines that the main source of error are bad image acquisition and more than 75% of missing information due to calcium shadowing. Two lines of research (currently in progress) are suggested to minimize the scope of erroneous detections. Taking into account periodicity in tissue movement in the point selection stage and mimicking the experts strategy for border interpolation at segments of significant lack of reliable information.

Acknowledgments

The authors would like to thank "Fundació Caixa Sabadell" and the projects FIS-G03/1085, FIS-PI031488, TIC2003-00654 for its support in making this work possible.

References

[1] D. Hausmann, A.J.S. Lundkvist, G. Friedrich, K. Sudhir, P.J. Fitzgerald and P.G. Yock, " Lumen and Plaque Shape in Atherosclerotic Coronary Arteries Assessed by In Vivo Intracoronary Ultrasound". *Am. J. Cardiol.*, vol. 74(9),pp.857–863, Nov. 1994.

[2] J. Dijkstra, G. Koning, J.C. Tuinenburg, P.V. Oemrawsingh, J.H.G. Reiber, "Automatic Border Detection in IntraVascular UltraSound Images for Quantitative Measurements of the Vessel, Lumen and Stent Parameters", *Computer Assisted Radiology and Surgery - CARS 2001*, International Congress Series 1230, pp. 916-922.

[3] C. von Birgelen, C. D. Mario, W. Li, J. C. Schuurbiers, C. J. Slager, P. J. de Feyter, J. R. Roelandt, and P. W. Serruys, "Morphometric analysis in three-dimensional intracoronary ultrasound: An in vitro and in vivo study performed with a novel system for the contour detection of lumen and plaque", *Amer. Heart J.*, vol. 132, pp. 516-527, 1996.

[4] C. von Birgelen, G. S. Mintz, A. Nicosia, D. P. Foley, W. J. van der Giessen, N. Bruining, S. G. Airiian, J. R. T. C. Roelandt, P. J. de Feyter, and P. W. Serruys, "Electrocardiogram-gated intravascular ultrasound image acquisition after coronary stent deployment facilitates on-line three-dimensional reconstruction and automated lumen quantification", *J. Amer. Coll. Cardiol.*, vol. 30, pp. 436-443, 1997.

[5] P.A. Brathwaite, K.B. Chandran, D.D. McPherson, E.L. Dove, " Lumen detection in human IVUS images using region-growing", *Computers in Cardiology 1996*, pp. 37–40.

[6] Zhongchi Luo, Yuanyuan Wang, and Weiqi Wang, "Estimating Coronary Artery Lumen Area With Optimization-Based Contour Detection", *IEEE Trans. Med. Imag.*, vol. 22, no. 4, pp. 564–566, 2003.

[7] E. Brusseau, C.L. de Korte, F. Mastik, J. Schaar, Anton F. W. van der Steen, "Fully Automatic Luminal Contour Segmentation in Intracoronary Ultrasound Imaging A Statistical Approach", *IEEE Trans. Med. Imag.*, vol. 23, no. 5, 2004.

[8] M. Sonka and X. Zhang and M. Siebes et al. "Segmentation of intravascular ultrasound images: A knowledge based approach", IEEE Trans. Med. Imag. vol.14: pp. 719–732, 1995.

[9] Mark E. Olszewski, Andreas Wahle, Steven C. Mitchell, Milan Sonka, "Segmentation of intravascular ultrasound images: a machine learning approach mimicking human vision", *CARS*, pp. 1045–1049, 2004.

[10] X. Zhang, M. Sonka, "Tissue characterization in intravascular ultrasound images", *IEEE Trans. Med. Imag.*, vol. 17, no.6, pp. 889–899, 1998.

[11] O. Pujol, P. Radeva, "Supervised Texture classification for Intravascular Tissue Characterization", in *Handbook of Medical Image Analysis: Advanced Segmentation and Registration Models*, pp. 57–110. Editorial: Kluwer Academic/ Plenum Publishers, 2005. ISBN: 0-306-48550-9.

[12] C. Haas, H. Ermert, S. Holt, P. Grewe, A. Machraoui, J. Barmeyer, "Segmentation of 3D intravascular ultrasonic images based on a random field model", *Ultrasound Med. Biol.*, vol. 26, no. 2, pp. 297–306, 2000.

[13] A. Takagi, K. Hibi, X. Zhang, T. J. Teo, H. N. Bonneau, P. G. Yock, P. J. Fitzgerald, "Automated contour detection for high-frequency IVUS imaging: a technique with blood noise reduction for edge enhancement", *Ultrasound Med. Biol.*, vol. 26, no. 6, pp. 1033–1041, 2000.

[14] M.E. Plissiti, D.I. Fotiadis, L.K. Michalis, G.E. Bozios, "An Automated Method for Lumen and Media-Adventitia Border Detection in a Sequence of IVUS Frames", *IEEE Trans. Information Tech. in Biomedicine*, vol. 8, no. 2, pp. 131–141, 2004.

[15] JD. Klingensmith, R. Shekhar, DG. Vince, "Evaluation of three-dimensional segmentation algorithms for the identification of luminal and Medial-adventitial borders in intravascular ultrasound", *IEEE Trans. Med. Imag.*, vol. 19, no.10, pp. 996–1011, 2000.

[16] J. Dijkstra, G. Koning and J.H.C. Reiber, "Quantitative measurements in IVUS images". *The International Journal of Cardiovascular Imaging*. vol. 15, no 6, pp. 513–522, 1999.

[17] A. Hernandez, D. Gil, P. Radeva, E. Nofrerias, "Anisotropic Processing of Image Structures for Adventitia Detection in IVUS Images", *IEEE Proc. CiC 2004*, vol. 31, pp. 229–232.

[18] W.F. Young, S. McLaughlin, "Pseudo-inverse filtering of IVUS images", *IEEE Proc. Science, Measurement and Technology*, vol. 145, Issue 6, pp. 321–326, 1998.

[19] M. Rosales, P. Radeva, "Simulation Model of Intravascular Ultrasound Images", *Med. Imag. Comp. and Computer-Assisted Inter. MICCAI 2004*, LNCS (3217),pp. 200–207, 2004.

[20] X.M. Pardo, P. Radeva, D. Cabello, "Discrimant snakes for 3D reconstruction of anatomical organs", *Med. Imag. Ana.*, vol. 7, pp. 293–310, 2003.

[21] D. Rotger, M. Rosales, J. Garca, O. Pujol, J. Mauri, P. Radeva, "ActiveVessel: A New Multimedia Workstation for IVUS and Angiography Fusion", *Proceedings of Computers in Cardiology*, vol. 30, pp. 65–69, Thessaloniki, Greece, September, 2003.

[22] F. Vilario, P. Radeva, "Cardiac Segmentation with Discriminant Active Contours", *Artificial Intelligence Research and Development*. IOS Press, pp:211–215, 2003.

[23] M. Kass, A. Witkin and D. Terzopoulos, "Snakes: Active Contour Models", *Int. Journal of Computer Vision*, vol. 1(4), pp. 321–331, 1987.

[24] M. Brejl, M. Sonka, "Object localization and border detection criteria design in edge-based image segmentation: automated learning from examples", *IEEE Trans. on Medical Imaging*, vol. 19 (10), pp. 973–985, October 2000.

[25] T. F. Cootes, A. Hill, C. J. Taylor, and J. Haslam, "Use of active shape models for locating structures in medical images", *Image Vision Comput.*, vol. 12, pp. 355365, 1994.

[26] V. Caselles, R. Kimmel, G. Sapiro, "Geodesic Active Contours", *Int. Journal of Computer Vision*, vol. 22, no.1, pp. 61–79, 1997.

[27] D. Gil, P. Radeva, "Extending Anisotropic Operators to Recover Smooth Shapes", *Comp. Vis. Imag. Unders.*, vol. 99, pp. 110–125, 2005.

[28] D. Gil, "Geometric Differential Operators for Shape Modelling", *PhD Tesis, Universitat Autonoma de Barcelona*, 2004 (available at http://www.cvc.uab.es/ debora/)

[29] R. Carmona, S. Zhong, "Adaptative smoothing respecting feature directions", *IEEE Trans. Image Proc.*, vol. 7, no. 3, 1998.

[30] J. Weickert, "A Review of Nonlinear Diffusion Filtering, Scale-Space Theory in Computer Vision", *LNCS*, Springer-Verlag, 1997.

[31] R. Duda, P. Hart, "Pattern Classification", *Wiley-Interscience*, 2001.

[32] L.C. Evans, "Partial Differential Equations", *Berkeley Math. Lect. Notes*, 1993.

[33] B. Jähne, "Spatio-temporal image processing". *Lecture Notes in Comp. Science*, vol. 751, Springer, 1993.

[34] D.R. Martin, C.C. Fowlkes, J. Malik, "Learning to detect natural image boundaries using local brightness, color and texture cues", *IEEE PAMI*, vol. 26, pp. 1-20, 2004.

[35] J.R. Landis, G.G. Koch, "The measurement of observer agreement for categorical data", *Biometrics*, vol. 33, pp.159174, 1977.

[36] G.S. Mintz, S.E. Nissen et al. "Clinical Expert Consensus Document on Standards for Acquisition, Measurement and Reporting of Intravascular Ultrasound Studies (IVUS)".*J. Am. Coll. of Card.*, vol. 37(5), pp. 1478–92, April 2001.

[37] G. Kanizsa, "Organization in Vision: Essays in Gestalt Continuation", *Praeger*, New York, 1979.